

LEADING-EDGE TUBERCLES APPLIED ONTO A FLAPPED RUDDER

Moritz Troll

Department of Naval
Architecture, Ocean & Marine
Engineering,
University of Strathclyde
Glasgow, UK

Weichao Shi

Department of Naval
Architecture, Ocean & Marine
Engineering,
University of Strathclyde
Glasgow, UK

Callum Stark

Department of Naval
Architecture, Ocean & Marine
Engineering,
University of Strathclyde
Glasgow, UK

ABSTRACT

The addition of a trailing edge flap is an effective way to enhance the lift generated by marine rudders. This is achieved through camber being introduced into the foil section when the flap is deflected. But the strong curvature in the flow around the flap's leading edge makes it prone to early flow separation and increased drag. Leading-edge tubercles offer a means to control flow separation whilst improving lifting performance at post-stall angles of attack (AOA). Therefore, this study aims to investigate the tubercle leading edge's (TLE) ability to improve the hydrodynamic performance of a flapped rudder. A finite-span reference rudder with a 20% trailing-edge flap and its TLE modification were numerically analysed using Detached Eddy Simulations (DES) for fully turbulent flow at a Reynolds number of 1.15×10^6 .

Flow separation severity and progression were controlled and minimised through the TLE modifications. As a result, the TLE rudder produced up to 15% higher maximum lift and up to 25% more post-stall lift. The rudder efficiency also improved for various rudder and flap angle combinations.

Keywords: Flapped Rudder, Leading-Edge Tubercles, Hydrofoil, Computational Fluid Dynamics, Detached Eddy Simulations

1. INTRODUCTION

Most ships today use movable control surfaces to safely manoeuvre and keep course during their voyages. These typically foil-shaped appendages include rudders, fin stabilisers, and hydroplanes, amongst others. Marine control surfaces (MCS) are designed to be effective, i.e., provide useful lifting force, and efficient to minimise drag and the associated fuel consumption [1].

One high-lift rudder concept is the flapped-rudder, an all-movable rudder with a mechanically or hydraulically actuated flap along the trailing edge (TE). This flap covers a certain percentage of the total rudder area, defined by the flap-area ratio, η (flap area/total rudder area). The flap is deflected at a flap angle (FA, δ) relative to the rudder chord. The relation between rudder angle of attack (AOA, α) and the FA is described by the flap-linkage ratio, ε (flap angle/rudder angle). As the rudder is turned, the flap introduces camber into the foil section which increases the lift curve slope, provide higher lift, and delay stall [2]. The increase in lift allows for greater manoeuvrability or for smaller rudders to be installed which would reduce drag and result in fuel savings. The steeper lift curve slope also provides a faster manoeuvring response [2].

Experimental studies in the 1960s and 1970s by Kato and Motora [3] and Kerwin et al. [4], [5] showed how flapped rudders enhanced lift by up to 70% and reduced drag when compared to all-movable rudders in similar lifting conditions. Whilst foil sections, planforms, aspect ratios (AR) varied between the studies, they all agreed that a flap-area ratio of $\eta = 20\text{-}25\%$ performed best, as well as recommending flap-linkage ratios of $\varepsilon = 1\text{-}2$ [3]–[5]. This was further confirmed in a numerical 2D RANS study by Liu et al. [6] who compared various rudder sections, flap-area ratios, and flap-linkage ratios, where a rudder with $\eta = 20\%$, $\varepsilon = 1.5$ gave the best performance regarding effectiveness and efficiency.

However, their study also highlighted how flow separation begins earlier and is more severe on the flap surface compared to an all-movable rudder, which leads to an increase in drag and overall reduction in lift-to-drag ratio compared to all-movable rudders [6]. To address these flow separation problems flapped rudders have been modified further to blown flap gap rudders, or rotating cylinder flapped

rudders, which modifies the boundary layer, maintaining flow attachment, and further enhancing lift [2]. However, these active flow control devices add large complexity to the design, installation, and maintenance of the rudder system.

A passive flow control device that has gained increasing attention in recent years is the Tubercle Leading Edge (TLE), a bio-inspired design mimicking the leading edge (LE) of Humpback whale (*megaptera novaeangliae*) pectoral flippers. These whales have great agility for their large body size, which is attributed to a series of distinctive bumps on their pectoral flippers, the so-called tubercles. Researchers studying a humpback whale fin replica with and without tubercles, as well as tubercle applications to various aero and hydrofoils, reported lift improvements in the pre-stall regime, and whilst in most cases the maximum lift coefficient was reduced, the tubercles led to a more gradual onset of stall and significant improvements in post-stall lift [7]–[10]. This is achieved through the formation of streamwise counter-rotating vortex pairs forming behind each tubercle, which exchange momentum in the flow and energise the boundary layer [11]–[13]. The streamwise vortex pairs compartmentalise the flow over the suction side, keeping the flow attached behind the tubercle crests, whilst small stall cells can be observed in the troughs [14]. The prolonged flow attachment over the crest sections up to high AOA makes the TLE’s superior post-stall performance possible.

The TLE concept has already been successfully applied to rudders and other marine applications, such as tidal turbine blades, propellers, or ducts, where it showed improved flow attachment, prolonged post-stall lift, as well as cavitation mitigation capabilities [9], [15]–[18].

On paper, the advantages TLE modifications offer (i.e., improved lift through flow separation control) have the potential to address the flapped rudder’s main weakness of early flow separation on the flap surface. A flapped rudder with TLE could maintain attached flow up to the TE for at least certain sections along the span, which could reduce its drag penalty, as well as further increase lift. The TLE has the potential to make flapped rudders more efficient and more effective. This paper therefore aims to investigate the effects of TLE applied onto a flapped rudder at a fully-turbulent Reynolds number (R_n). The study employs a numerical approach, solving the hydrodynamic flow field via Detached Eddy Simulations (DES) in the commercial Computational Fluid Dynamics (CFD) code STAR-CCM+.

2. REFERENCE RUDDER AND MODIFICATIONS

The first requirement of the study was to find a suitable reference model of a flapped rudder with experimental data available that the numerical model could be validated against. Kerwin et al. [5] presented a comprehensive data set for a finite-span flapped rudder tested over a range of AOA and FA. In their study a model-scale rudder was analysed in a water tunnel for a Reynolds number of $R_n \approx 1.15 \times 10^6$ based on nominal chord length (C_{nom}).

2.1 Flapped Rudder Model

The rudder model chosen for this study is a replica of the $\eta = 20\%$ rudder presented in above mentioned study [5], as the larger flap showed a more significant improvement in lift. The rudder profile is modelled after a NACA 632A015 section with the suction side mirrored. The profile was further modified to maintain a constant section across the TE flap as described in [5]. The main rudder parameters are stated in Table 1 and displayed in Figure 1. An idealised setup was adopted for the numerical simulations where the main part of the rudder and the flap are joined together to form a single solid body, thereby neglecting any disturbances caused by the flap gap.

TABLE 1: MAIN PARAMETERS OF REFERENCE RUDDER

Parameter	Symbol	Unit	Value
Span	S	m	0.200
Nominal Chord	C_{nom}	m	0.143
Root Chord	C_{root}	m	0.179
Tip Chord	C_{tip}	m	0.107
Geometric Aspect Ratio	ARG	-	1.40
Taper Ratio	TR	-	0.60
Sweep Angle	Ω	deg.	15.0

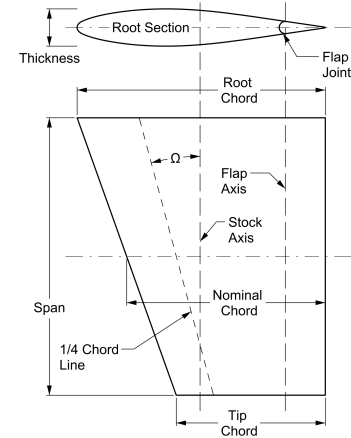


FIGURE 1: REFERENCE RUDDER GEOMETRY DEFINITION

2.2 Tubercle Leading Edge

The TLE was designed to follow a sinusoidal waveform oscillating about the LE of the reference ruder. The tubercle amplitude was fixed at $5\% C_{nom}$ and the wavelength at $36\% C_{nom}$ resulting in 4 tubercles covering the LE. This geometry configuration performed well in a previous study by the authors [18] investigating an all-movable rudder of similar planform shape and foil section. Furthermore the TLE was designed in a “crest configuration” where it terminates on a crest at the rudder tip, which can minimise the tip vortex generation [19]. The straight leading-edge rudder will hereinafter be referred to as SLE and the tubercle leading edge rudder as TLE4. Both rudder geometries can be seen in Figure 2.

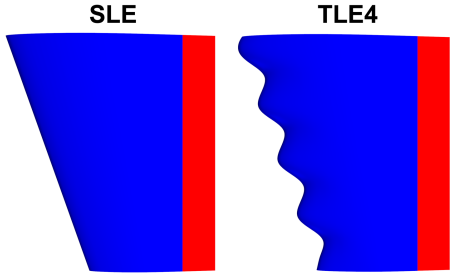


FIGURE 2: RUDDER GEOMETRIES WITH MAIN RUDDER SURFACE (BLUE) AND TRAILING EDGE FLAP (RED)

3. NUMERICAL SETUP

3.1 Computational Domain

The computational domain was cuboid shaped with the velocity inlet and pressure outlet boundaries placed $5 C_{nom}$ and $15 C_{nom}$ upstream and downstream from the LE and TE, respectively. The rudder was placed vertically centred on the right-hand-side boundary with a $5 C_{nom}$ clearance above and below. The domain width was set equal to $7 C_{nom}$. The rudder surface itself was defined as a no-slip wall. The results of the experimental reference study had to be corrected for boundary layer effects from the rudder endplate [5]. To avoid any boundary layer effects the right-hand-side boundary was defined with a symmetry plane condition and without any gap between the rudder and the boundary surface. The top, bottom, and left boundary were set as slip walls. The domain and respective boundary conditions are displayed in Figure 3.

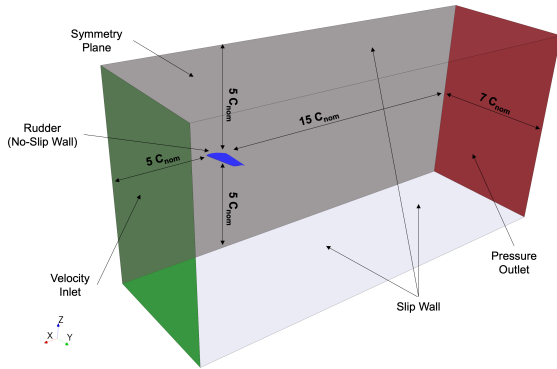


FIGURE 3: COMPUTATIONAL DOMAIN SIZING AND BOUNDARY CONDITIONS

3.2 Mesh Generation

The mesh was generated using the polyhedral mesher. A prism layer mesh was created around the rudder surface to resolve the boundary layer. It was tailored to the low y^+ wall treatment model, using 22 prism layers with a growth factor of ≈ 1.3 to target a wall $y^+ < 1$. The rudder surface was meshed with a uniform surface mesh. The flap surface mesh was further refined to better capture the expected flow separation. Target surface mesh sizes were ≈ 1.0 mm and ≈ 0.5 mm for the rudder

and flap surfaces, respectively. Volumetric refinements with 12.5% and 50% C_{nom} offsets were created around the main rudder and flap surface to accurately resolve the flow field around the rudder. Additional refinements were added in the wake area of the rudder. The final mesh had an approximate cell count of 18.8 million. The surface, boundary layer, and volume mesh for one example case can be seen in Figure 4.

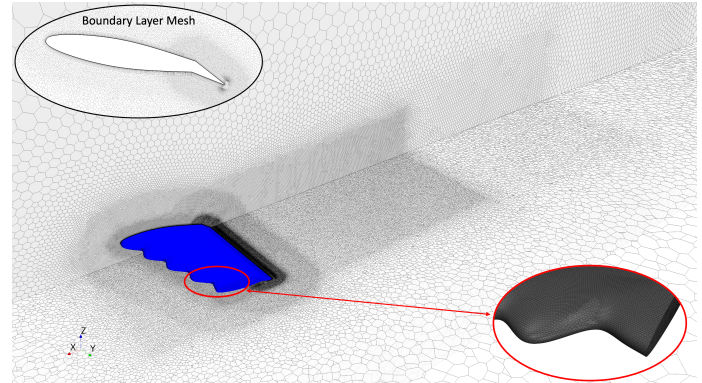


FIGURE 4: EXAMPLE OF SURFACE, BOUNDARY LAYER, AND VOLUME MESH

3.3 Numerical Solvers

The Improved Delayed Detached Eddy Simulation (IDDES) solver was chosen to resolve the hydrodynamic flow field. This hybrid LES-RANS approach is highly applicable to hydrodynamic problems analysing separated flow, as DES has superior capabilities of resolving separation without the need for excessive computational resources. Several researchers already reported good results for numerical analyses of TLE using DES [12], [13]. Incompressible segregated SIMPLE flow solvers with a hybrid second-order upwind / bounded-central differencing discretisation schemes were used. The shear stress transport (SST) $k-\omega$ turbulence model was chosen due to its superior capabilities of capturing the more complex separated flows [13]. Simulations were set up to be implicit unsteady with second-order temporal discretisation and the time step (Δt) was calculated as

$$\Delta t = \Delta_0 / V_{max} \approx 1.0e^{-4} s \quad (1)$$

where Δ_0 (m) is the smallest grid cell length (m) and V_{max} is an estimate of the highest flow velocity (m/s) within the flow region of interest [20]. 9 inner iterations were run for each time step.

3.4 Test Matrix

To be able to assess the effect of the TLE modifications a range of conditions was considered. The AOA range covered the linear lifting regime, maximum lift condition, and stall, where the largest effect from the TLE was expected. For each condition the neutral flap position and two FA ($\delta=10^\circ, 20^\circ$) were simulated. Additionally, the zero-lift condition for both rudder models was added to assess the impact of the TLE when no lift is generated. The full test matrix can be seen in Table 2 below.

TABLE 2: TEST MATRIX

Angle of Attack	Flap Angle	Test Condition
α	δ	-
0°	0°	Zero Lift Condition
10°	0°, 10°, 15°	Linear Lifting Regime
15°	0°, 10°, 15°	
20°	0°, 10°, 15°	Maximum Lift Condition
25°	0°, 10°, 15°	Post-stall Regime

4. VALIDATION OF THE NUMERICAL MODEL

4.1 Performance Coefficients

Any numerical model needs to be validated to be confident in the results it generates. The two main indicators for the performance of hydrofoils are the lift and drag coefficients, C_L and C_D respectively, which are defined as follows:

$$C_L = \frac{2L}{\rho V^2 A} = \frac{2L}{\rho V^2 S \times C_{nom}} \quad (2)$$

$$C_D = \frac{2D}{\rho V^2 A} = \frac{2D}{\rho V^2 S \times C_{nom}} \quad (3)$$

where L and D are the lift and drag forces (N), ρ is the fluid density (kg/m^3), and A is the lifting area (m^2) calculated as the product of the span (S) and C_{nom} .

The simulations were run at the fully-turbulent Reynolds number, $R_n = 1.15 \times 10^6$, of the experimental reference study [5], equivalent to a free-stream velocity (V) of $V = 9.571$ m/s. The flow residence time in the domain at this velocity is calculated as

$$L_{domain}/V = 0.31 \text{ s} \quad (4)$$

where L_{domain} is the total computational domain length (m). To achieve statistical steadiness of the solution and for time-averaged results to be taken a run time of approximately 0.6 s (twice the flow residence time) was targeted, with several simulations converging much sooner.

The simulations were run on single nodes of the *ARCHIE-WeSt* Research Computing Centre with 40 2.0 GHz Intel Xenon Gold 6138 CPU cores per node. The target simulation times were achieved in approximately 140 hours run time or 5500 CPU hours.

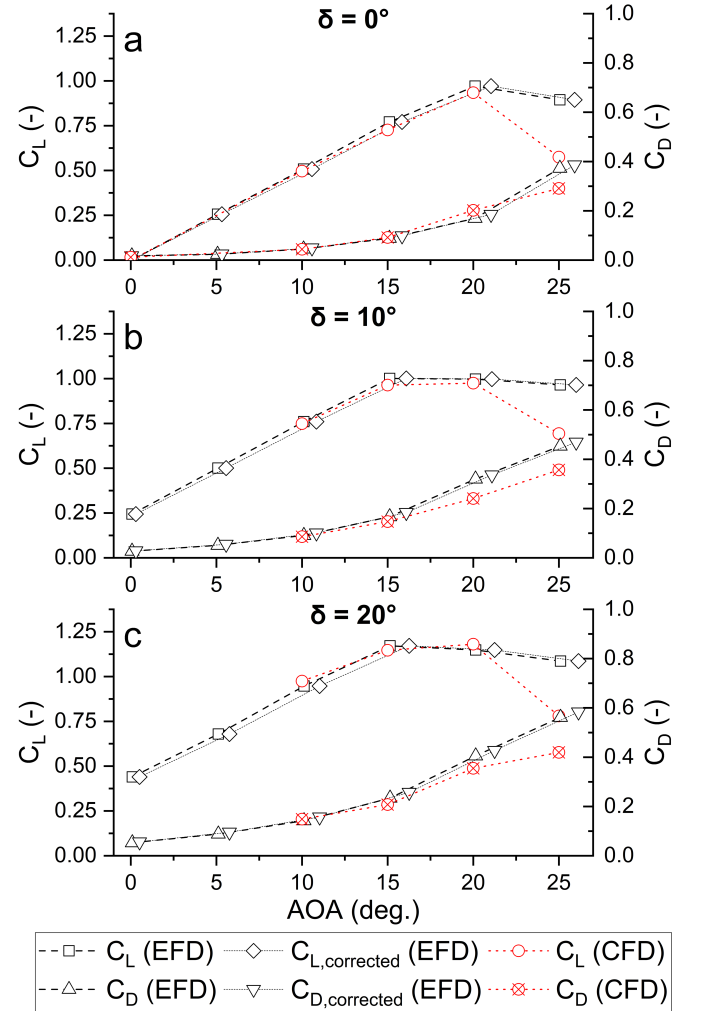
4.2 Mesh Convergence

A mesh independence study was performed for the SLE rudder with $\alpha = 15^\circ$, $\delta = 10^\circ$. The Grid Convergence Index (GCI) method described in Celik et al. [21] was employed. This method, based on Richardson extrapolation, compares the results of a critical variable (ϕ_i) obtained from three progressively refined meshes (N_i) and calculates the numerical uncertainty

when changing from a coarse to the next finer mesh. C_L and C_D were chosen as critical variables. The GCI results are presented in Table 3 below. The uncertainty of both variables for the 18.8m cell mesh, GCI_{21} , was below 0.5% and deemed sufficiently small.

TABLE 3: GRID CONVERGENCE INDEX ANALYSIS FOR SLE AT $\alpha = 15^\circ$, $\delta = 10^\circ$

Critical Variable	ϕ_1 ϕ_2 ϕ_3	N_1 N_2 N_3	GCI_{32}	GCI_{21}
C_L	0.9637	18,800,000	1.974%	0.433%
	0.9520	8,200,000		
	0.9045	3,800,000		
C_D	0.1469	18,800,000	2.300%	0.379%
	0.1492	8,200,000		
	0.1618	3,800,000		


FIGURE 5: CFD PERFORMANCE COEFFICIENT RESULTS COMPARISON AGAINST EXPERIMENTAL REFERENCE STUDY AT $R_N = 1.15 \times 10^6$

4.3 Hydrodynamic Validation against Experimental Reference Study

The SLE simulation results (denoted CFD) for all conditions outlined in Table 2 were then compared against the experimental results (denoted EFD) presented in Kerwin et al. [5]. The validation study results are presented in Figure 5.

The numerical results are in good agreement with the experiments. The only notable discrepancies can be seen at the highest AOA, where the CFD model predicts more severe flow stall compared to the EFD results, which is a common limitation of CFD. Nevertheless, since the SLE and TLE rudders were to be compared using the same numerical setup which also showed small numerical uncertainty, the numerical model was deemed to be sufficiently accurate.

5. RESULTS

5.1 Performance Coefficient Comparison

First, the hydrodynamic coefficients of the SLE and TLE4 rudders were compared. The comparison results are plotted in Figure 6. In Fig. 6a, where $\delta = 0^\circ$, the rudders are essentially all-movable rudders. The typical performance of a finite-span hydrofoil with TLE can be observed here. In the pre-stall regime at $\alpha = 10^\circ$ TLE4 and SLE are matched. C_L increases slightly for $\alpha = 15^\circ$ before the lift curve of TLE4 flattens off and C_{Lmax} is slightly reduced compared to SLE. However, lift is maintained all the way up to $\alpha = 25^\circ$, where the SLE rudder is stalled and has a 30% smaller C_L . C_D increases visibly for TLE4 for stall and post-stall AOA 20° and 25° . The increase in lift at the highest AOA outweighs the drag penalty, increasing lift-to-drag ratio (L/D) for TLE4, making this rudder configuration more efficient.

Comparing the hydrodynamic performance when the flap is deflected for $\delta = 10^\circ$ (Fig. 6b) and $\delta = 20^\circ$ (Fig. 6c), the performance of TLE4 for $\alpha = 15^\circ$ stands out. At this AOA the TLE increases C_L by 14% and 10% over the SLE rudder for $\delta = 10^\circ$ and $\delta = 20^\circ$, respectively. Furthermore, for $\delta = 10^\circ$, C_{Lmax} is shifted from $\alpha = 20^\circ$ to $\alpha = 15^\circ$ for TLE4, where it generates more lift and less drag compared to the C_{Lmax} condition of the SLE rudder, thereby increasing the effectiveness and efficiency significantly. As the AOA is increased, the lift curve of TLE4 drops off and flattens out. At $\alpha = 20^\circ$, TLE4 exhibits a small lift penalty for $\delta = 10^\circ$ and $\delta = 20^\circ$. At $\alpha = 25^\circ$ the SLE rudder has stalled and C_L drops. TLE4 on the other hand largely maintains its C_L values past stall and generates 25% and 18% more lift than SLE for $\delta = 10^\circ$ and $\delta = 20^\circ$, respectively. This post-stall lift performance is typical for aero or hydrofoils with TLE. Whilst lift is largely improved, TLE4 also shows a drag penalty at the higher AOA for $\delta = 10^\circ$ and $\delta = 20^\circ$. This reduces the rudder efficiency for $\alpha = 20^\circ$, but at $\alpha = 25^\circ$ the gains in lift outweigh the drag penalty and the efficiency is improved. Generally, the TLE modifications applied to the flapped rudder have shown an increase in peak effectiveness for all FA deflections, as well as efficiency improvements in certain operating conditions.

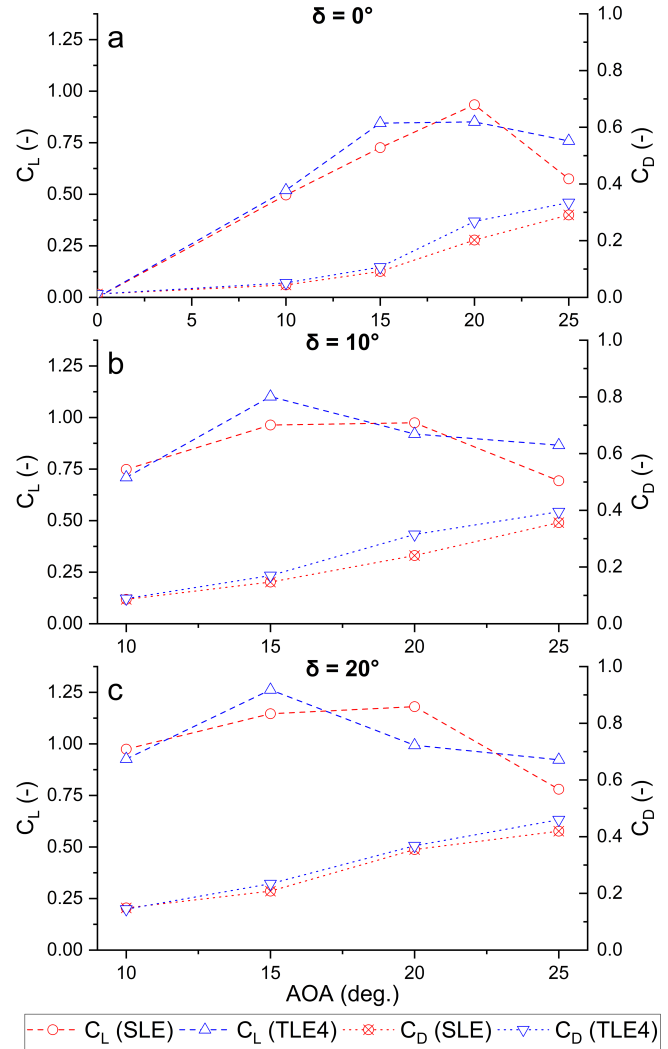


FIGURE 6: PERFORMANCE COEFFICIENT COMPARISON BETWEEN SLE AND TLE4 AT $R_N = 1.15 \times 10^6$

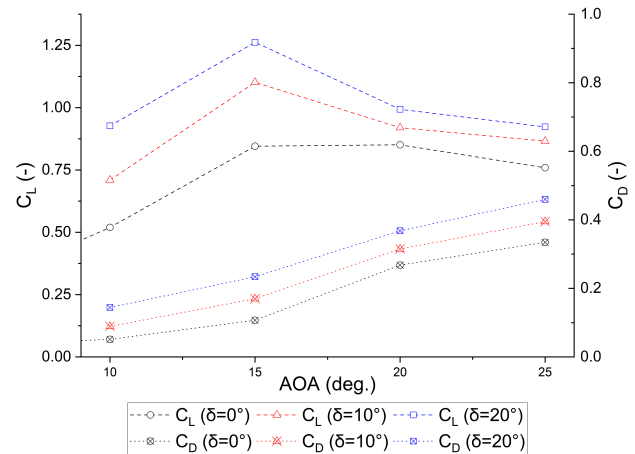


FIGURE 7: FLAP ANGLE EFFECT FOR TLE4 AT $R_N = 1.15 \times 10^6$

Comparing the 3 different FA for TLE4 in Figure 7, it can be seen how the TLE flapped rudder performs similarly to conventional flapped rudders. For increasing FA, the C_L and C_D curves increase. For $\alpha = 20^\circ, 25^\circ$, C_L increases by constant margins as FA increases. Improvements are larger for C_L at $\alpha = 10^\circ$, but most significantly at $\alpha = 15^\circ$, where $C_{L,max}$ is increased by 30% and 50% from 0.845 to 1.102 and 1.262 for $\delta = 10^\circ$ and $\delta = 20^\circ$, respectively. The improvement in C_L for $\alpha = 15^\circ, \delta = 20^\circ$, where $\varepsilon = 1.33$ corresponds well with previous researchers' findings who stated flap-linkage ratios around 1.5 to be optimal.

The differences in hydrodynamic coefficients were most notable for $\alpha = 15^\circ$. Therefore, the further discussion of results will mainly focus on the analysis of this angle.

5.2 Formation of Tubercle Streamwise Counter-Rotating Vortex Pairs

Prior to disseminating how the TLE flapped rudder achieved its performance advantage, it is important to explain the main flow mechanisms that differentiate the TLE from the straight LE. Figure 8 shows streamwise vorticity scalars plotted on spanwise cut planes distributed over the suction side surfaces of SLE and TLE4 for the example case of $\alpha = 10^\circ, \delta = 0^\circ$.

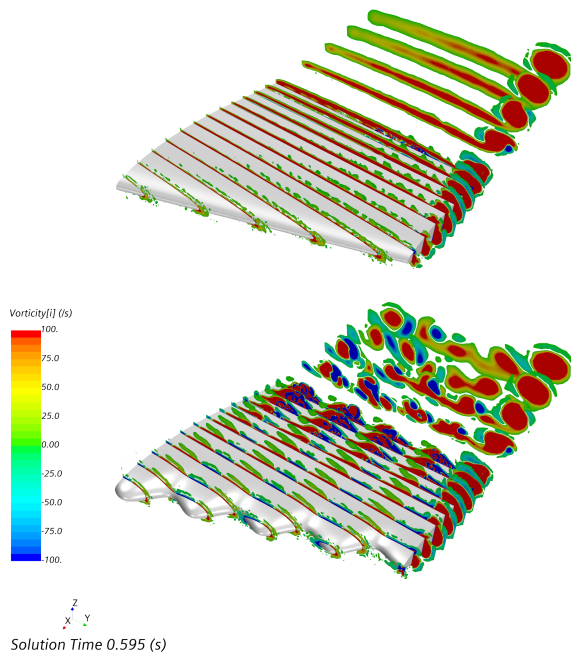


FIGURE 8: FORMATION OF STREAMWISE COUNTER-ROTATING VORTEX PAIRS OVER TLE RUDDER FOR EXAMPLE CASE $\alpha = 10^\circ, \delta = 0^\circ$

The formation of the streamwise counter-rotating vortex pairs behind each individual tubercle can clearly be seen. The vortices change the pressure distribution over the suction side surface which leads to prolonged flow attachment over tubercle crest sections, whilst flow separates early behind the troughs where small, localised stall cells form. The vortices themselves strengthen further around these stall cells. A second effect of the

vortices is that they compartmentalise flow and limit the spanwise progression of flow separation typical for aero and hydrofoils with straight LE. The formation of the streamwise counter-rotating vortices was observed for all TLE cases analysed.

5.3 Flow Separation Behaviour

The following section investigates the flow separation behaviour of the flapped rudder and how it was affected by the TLE modifications. The flow separates from the rudder surface when the streamwise velocity becomes zero or negative. Iso-surfaces capturing the flow regions around the rudder with zero or negative streamwise flow velocities were set up.

Figure 9 shows the flow separation progression from $\delta = 0^\circ$ (left) to $\delta = 10^\circ$ (middle) and 20° (right) of the SLE rudder model at $\alpha = 10^\circ$. Flap deflection induces camber and generates larger pressure differences between rudder suction and pressure side, thereby generating more lift [6]. However, the sudden change in curvature around the flap linkage makes it difficult for the flow to remain attached. This can be seen from the increasing flow separation as FA increases in Figure 9.

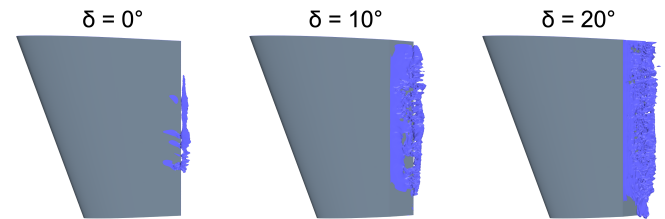


FIGURE 9: ISOSURFACE VISUALISATION OF ZERO STREAMWISE FLOW VELOCITY HIGHLIGHTING FLOW SEPARATION BEHIND SLE RUDDER MODEL AT $\alpha = 10^\circ$

Figure 10 compares the flow separation patterns of the SLE (left) and TLE4 rudder (right) at $\alpha = 15^\circ$ for $\delta = 0^\circ, 10^\circ, 20^\circ$. In Fig. 10a it can be seen how the flow separation that started centralised on the TE has spread out spanwise and started progressing towards the LE. Similarly, for $\delta = 10^\circ, 20^\circ$ in Fig. 10c, 10e separation now spans across the entire flap area and is progressing onto the suction side of the main rudder part. This kind of separation is associated with increased drag, which can be seen in Figs. 5, 6. Flow separation also leads to a loss of lift. However, at these intermediate AOA the lift gained from increase in pressure difference between rudder sides as AOA increases outweighs the lift penalty from separation progression.

The separation patterns of the TLE4 rudder at $\alpha = 15^\circ$ in Fig. 10b, d, f are vastly different compared to the SLE rudder. It can be seen how the tubercle streamwise counter-rotating vortices successfully compartmentalised the flow and limited the formation of full spanwise separation. Instead, small stall cells have formed downstream of the troughs of the individual tubercles. The areas downstream from the tubercle crest in Fig. 10b show almost no signs of separated flow.

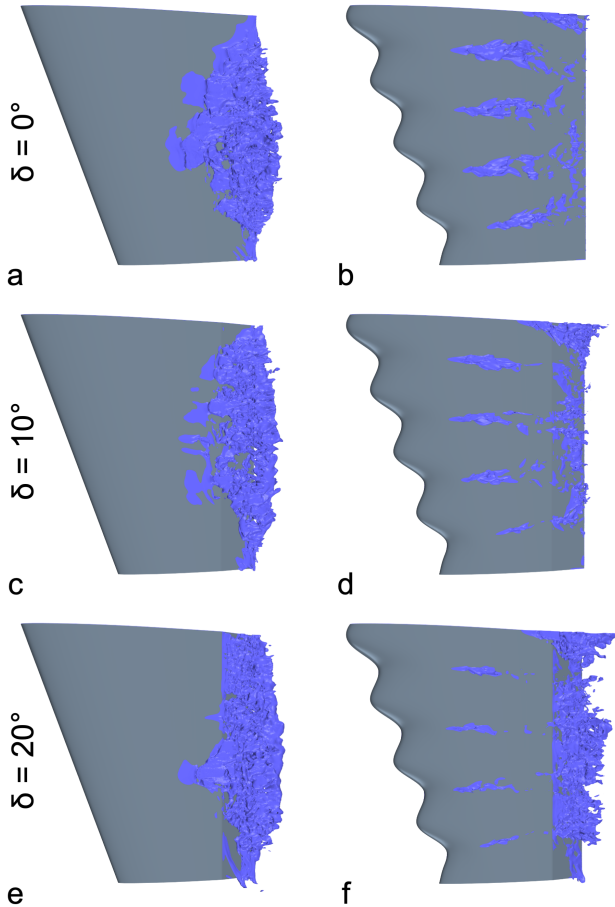


FIGURE 10: ISOSURFACE VISUALISATION OF FLOW SEPARATION BEHIND RUDDER MODELS AT $\alpha = 15^\circ$

Comparing Fig. 10c and 10d it can be seen how the TLE modification managed to keep flow attached over a large part of the TE flap. This leads to a larger area of the TLE4 rudder acting as a cambered foil with fully attached flow, and the rudder generating 14% more lift than its SLE counterpart. The effect is similar for $\delta = 20^\circ$ (see Fig. 10f) but less pronounced, due to the naturally larger separation along the flap in this case. Nevertheless, the separated wake is much smaller compared to the SLE in this configuration (see Fig. 10e) which again is reflected in a 10% increase in C_L .

Interestingly, there appears to be a relation between the stall cells in the tubercle troughs and the separation severity along the flap. The two seem to be decoupled as smaller tubercle stall cells form for higher flap separation for the larger FA, and vice-versa.

As discussed in Section 5.1, when the AOA is increased further to $\alpha = 20^\circ$, the performance of the TLE4 rudder dips and it less effective and efficient than the SLE rudder. Then the SLE rudder fully stalls at $\alpha = 25^\circ$ and the performances are reversed by the more gradual stall onset of TLE4. This can also be explained when comparing the separation behaviour of the two

rudders at these angles, as shown in Figure 11 for the example case of $\delta = 10^\circ$. Whilst the TLE confines the large separation area between tubercles 3 and 4 at $\alpha = 20^\circ$, lift is compromised due to early flow separation in the trough areas between tubercles 1 and 2. As a result of this, TLE4 is outperformed by SLE.

At $\alpha = 25^\circ$ however, the flow over SLE separates right at the LE. The flow over the rudder is fully stalled resulting in the drastic loss of lift. The same holds true for the majority of the TLE4 rudder surface, but the tubercle vortices generated over tubercles 1 and 2 maintain attached flow in the root section. It is in this area, where the lift generated is closest to two-dimensional and therefore the local C_L is higher compared to anywhere else along the span. This results in the significant 25% increase in C_L and 13% increase in L/D for TLE4 compared to SLE at this angle.

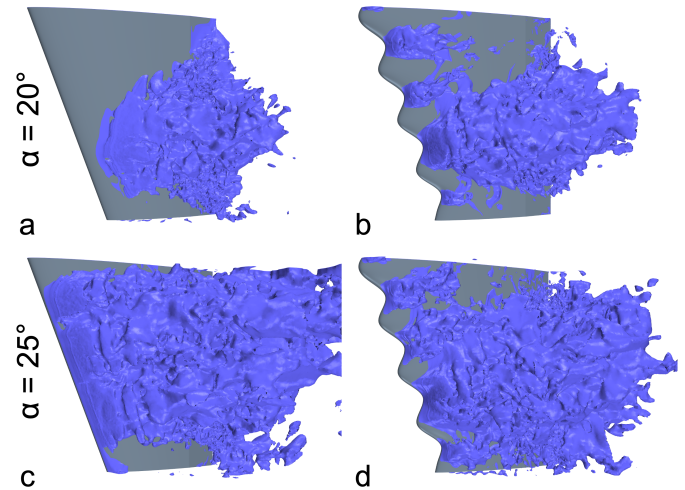


FIGURE 11: ISOSURFACE VISUALISATION OF FLOW SEPARATION BEHIND RUDDER MODELS WITH $\delta = 10^\circ$

1. CONCLUSION

A representative flapped rudder model was modified with leading-edge tubercles and numerically modelled for a range of AOA and FA for a fully-turbulent Reynolds number of 1.15×10^6 using DES. The hydrodynamic performance of the two models, as well as the flow separation behaviour were analysed and compared. The following conclusions can be drawn:

1. Flapped rudders can benefit from TLE modifications as their effectiveness and / or efficiency can be improved for a variety of AOA and FA combinations.
2. TLE modifications further increased the maximum lift coefficient by up to 15% when the TE flap is deflected. C_{Lmax} is also shifted to lower AOA where the rudder generates less drag and therefore efficiency was improved.
3. The performance improvements were facilitated by the TLE limiting flow separation severity and progression in the pre- and post-stall regime of the reference rudder.

ACKNOWLEDGEMENTS

The results were obtained using the University of Strathclyde's High Performance Computer ARCHIE-WeSt (<https://www.archie-west.ac.uk/>). This work was supported by BAE systems plc. (Ref: MEIR PhD 17), which is greatly appreciated and acknowledged.

REFERENCES

- [1] J. Liu and R. Hekkenberg, "Sixty years of research on ship rudders: effects of design choices on rudder performance," *Ships Offshore Struct.*, vol. 12, no. 4, pp. 495–512, 2017.
- [2] A. F. Molland and S. R. Turnock, *Marine Rudders and Control Surfaces: Principles, Data, Design and Applications*. Elsevier/Butterworth-Heinemann, 2007.
- [3] H. Kato and S. Matora, "Studies on Rudders with Flap," *J. Soc. Nav. Archit. Japan*, vol. 1968, no. 124, pp. 93–104, 1968.
- [4] J. E. Kerwin, P. Mandel, and S. D. Lewis, "Hydrodynamic Characteristics of Flapped Rudders," *J. Mech. Eng. Sci.*, vol. 14, no. 7, pp. 142–149, Dec. 1972.
- [5] J. E. Kerwin, S. D. Lewis, and B. W. Oppenheim, "Experiments on rudders with small flaps in free-stream and behind a propeller," Boston, Massachusetts, U.S., 1974.
- [6] J. Liu, R. Hekkenberg, and B. Zhao, "RANS Study on Hydrodynamic Characteristics of Flapped Rudders," *Proc. Int. Conf. Offshore Mech. Arct. Eng. - OMAE*, vol. 11B, Sep. 2018.
- [7] D. S. Miklosovic, M. M. Murray, and L. E. Howle, "Experimental Evaluation of Sinusoidal Leading Edges," *J. Aircr.*, vol. 44, no. 4, pp. 1404–1408, 2007.
- [8] M. J. Stanway, "Hydrodynamic effects of leading-edge tubercles on control surfaces and in flapping foil propulsion," Massachusetts Institute of Technology, Massachusetts Institute of Technology, 2008.
- [9] P. W. Weber, L. E. Howle, and M. M. Murray, "Lift, Drag, and Cavitation Onset On Rudders With Leading-edge Tubercles," *Mar. Technol.*, vol. 47, no. 1, pp. 27–36, 2010.
- [10] D. Custodio, C. W. Henoeh, and H. Johari, "Aerodynamic Characteristics of Finite Span Wings with Leading-Edge Protuberances," *AIAA J.*, vol. 53, no. 7, 2015.
- [11] F. E. Fish, L. E. Howle, and M. M. Murray, "Hydrodynamic flow control in marine mammals," *Integr. Comp. Biol.*, vol. 48, no. 6, 2008.
- [12] H. T. C. Pedro and M. H. Kobayashi, "Numerical Study of stall delay on humpback whale Flippers," in *46th AIAA Aerospace Sciences Meeting and Exhibit*, 2008.
- [13] A. K. Malipeddi, N. Mahmoudnejad, and K. A. Hoffmann, "Numerical Analysis of Effects of Leading-Edge Protuberances on Aircraft Wing Performance," *J. Aircr.*, vol. 49, no. 5, pp. 1336–1344, 2012.
- [14] N. Rostamzadeh, K. L. Hansen, R. M. Kelso, and B. B. Dally, "The formation mechanism and impact of streamwise vortices on NACA 0021 airfoil's performance with undulating leading edge modification," *Phys. Fluids*, vol. 26, no. 107101, pp. 1–22, 2014.
- [15] H. S. Yoon, P. A. Hung, J. H. Jung, and M. C. Kim, "Effect of the wavy leading edge on hydrodynamic characteristics for flow around low aspect ratio wing," *Comput. Fluids*, no. 49, pp. 276–289, 2011.
- [16] W. Shi, M. Atlar, R. Rosli, B. Aktas, and R. Norman, "Cavitation observations and noise measurements of horizontal axis tidal turbines with biomimetic blade leading-edge designs," *Ocean Eng.*, vol. 121, pp. 143–155, Jul. 2016.
- [17] C. Stark, W. Shi, and M. Troll, "Cavitation funnel effect: Bio-inspired leading-edge tubercle application on ducted marine propeller blades," *Appl. Ocean Res.*, vol. 116, p. 102864, Nov. 2021.
- [18] M. Troll, W. Shi, and C. Stark, "The influence of leading-edge tubercles on wake flow dynamics of a marine rudder," in *9th Conference on Computational Methods in Marine Engineering*, 2021.
- [19] M. D. Bolzon, R. M. Kelso, and M. Arjomandi, "Performance effects of a single tubercle terminating at a swept wing's tip," *Exp. Therm. Fluid Sci.*, vol. 85, pp. 52–68, Jul. 2017.
- [20] P. R. Spalart, "Young-Person's Guide to Detached-Eddy Simulation Grids," Hampton, Virginia, US, 2001.
- [21] I. B. Celik, U. Ghia, P. J. Roache, C. J. Freitas, H. Coleman, and P. E. Raad, "Procedure for Estimation and Reporting of Uncertainty Due to Discretization in CFD Applications," *J. Fluids Eng. Trans. ASME*, vol. 130, no. 7, Jul. 2008.